

Transparent Conductive Oxide-Free Graphene-Based Perovskite Solar Cells with over 17% Efficiency

Hyangki Sung, Namyoung Ahn, Min Seok Jang, Jong-Kwon Lee, Heetae Yoon, Nam-Gyu Park, and Mansoo Choi*

Organic/inorganic hybrid perovskites are promising materials for use in photoactive layers of solar cells due to their unique properties such as high absorption coefficient, balanced electron/hole mobility, possible low-temperature processing, smaller exciton binding energy, and longer exciton diffusion length than those of organic semiconducting materials.^[1–9] The perovskite solar cells with high performances have usually adopted n–i–p architecture consisting of scaffold metal oxide such as TiO₂ or Al₂O₃/perovskite material/hole transport material.^[9–11] For the preparation of the metal oxide films, however, high-temperature process over 450 °C is required, which limits substrate choice and is not compatible with the low-cost manufacturing.

As an alternative to the metal oxide layers, organic materials have been utilized to perovskite solar cells, generally with p–i–n architecture. Here solution-processable poly(3,4-ethylenedioxythiophene):poly(styrenesulfonate) (PEDOT:PSS) and [6, 6]-phenyl C61-butyric acid methyl ester (PCBM) have been commonly used for a hole transport layer (HTL) and an electron transport layer (ETL), respectively.^[5,12–14] Very recently, 18.1% power conversion efficiency (PCE) has been achieved with p–i–n devices comprising indium tin oxide (ITO)/PEDOT:PSS/CH₃NH₃PbI₃ (MAPbI₃)/PCBM/gold (Au),^[15] which is still low compared to the n–i–p devices employing scaffold metal oxide for ETLs. Nevertheless, p–i–n perovskite solar cells have attracted much research interest due to their advantages of low hysteresis behavior, low processing temperature, and facile manufacturing process.^[14,15]

Taking advantage of the low-temperature processes, perovskite solar cells with p–i–n architecture have been employed on flexible substrates^[5,13] where ITO on plastic substrates has been mostly used as a transparent anode. However, it was found that ITO generated cracks and induced fracture under bending condition due to its mechanical brittleness.^[16] Meanwhile, there

have already been a lot of studies on bendable conducting electrodes in the field of organic photovoltaics (OPVs) to replace brittle transparent conductive oxides (TCOs) for flexible solar cell applications, such as graphene,^[17–20] carbon nanotubes,^[21–23] metal grids,^[24–26] and conductive polymers.^[27,28] Among them, graphene, a single-layer 2D carbon material, would be the most promising candidate because it is optically highly transparent (about 97% in visible range), mechanically robust, flexible, and stretchable. TCO-free OPV devices with graphene anode have already been successfully demonstrated showing a PCE of 8.48%, the highest efficiency for the TCO-free tandem polymer solar cells,^[20] although still lower than 11.0% PCE of the TCO-free perovskite solar cells.^[29] Graphene electrodes also have been recently employed in perovskite devices;^[30,31] however, in these studies, graphene was not used for replacing the conventional TCO electrode but for a top electrode.

Here we report highly efficient TCO-free inverted perovskite solar cells consisting of graphene/molybdenum trioxide (MoO₃)/PEDOT:PSS/MAPbI₃/fullerene (C₆₀)/bathocuproine (BCP)/lithium fluoride (LiF)/aluminum (Al). A few nanometer thick MoO₃ layers are employed between the graphene and PEDOT:PSS layers, similar to the OPVs adopting graphene as an anode,^[18] which provides hydrophilicity to the graphene surface and elevates its lower work function (4.23 eV) to a higher level (4.71 eV) by hole doping of graphene. The wettability of PEDOT:PSS and the device properties are affected by the thickness of the MoO₃ layer, and, as a result, best PCE of 17.1% is achieved with the graphene-based devices incorporating a 2 nm thick MoO₃ interfacial layer. For comparison, ITO-based perovskite solar cells employing MoO₃ interfacial layers have been also fabricated. Their PCEs also vary with the thickness of the MoO₃ layer, showing the best PCE of 18.8% with a 1 nm thick MoO₃ layer. The effects of the MoO₃ thickness on PCEs of the graphene- and the ITO-based devices are thoroughly investigated by analyzing hydrophilicity of electrode surfaces, electrode work functions, surface morphologies of constitutive films, and device properties.

The structure of the devices is schematically illustrated in Figure 1. We adopted an inverted MAPbI₃ perovskite solar cell structure using PEDOT:PSS and C₆₀/BCP as the HTL and the ETL, respectively, because the structure is low-temperature processable and thus suitable for future application on flexible plastic substrates. A single layer graphene, grown by chemical vapor deposition (CVD), was utilized as a transparent anode rather than a cathode because increasing its work function (≈4.3 eV) by p-doping induced not only an enhanced conductivity but also a desirable energy level alignment with the highest occupied molecular orbital level of HTLs (≈5.2 eV for PEDOT:PSS, for example). Between the graphene and the

H. Sung, N. Ahn, H. Yoon, Prof. M. Choi
Department of Mechanical and Aerospace Engineering
Seoul National University
Seoul 08826, South Korea
E-mail: mchoi@snu.ac.kr

Dr. M. S. Jang, Dr. J.-K. Lee, Prof. M. Choi
Global Frontier Center for Multiscale Energy Systems
Seoul National University
Seoul 08826, South Korea

Prof. N.-G. Park
School of Chemical Engineering
and Department of Energy Science
Sungkyunkwan University
Suwon 16419, South Korea

DOI: 10.1002/aenm.201501873



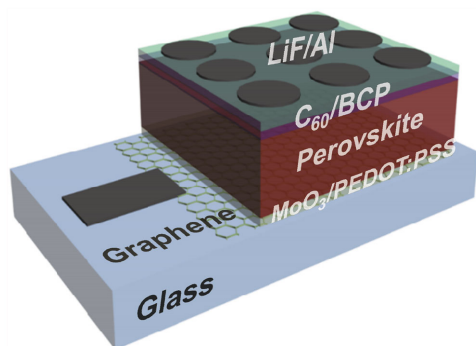


Figure 1. Schematic structure of the inverted MAPbI₃ perovskite solar cells utilizing graphene as a transparent anode.

PEDOT:PSS film, we added a MoO₃ layer by vacuum thermal evaporation, followed by thermal annealing at 150 °C on a hot plate to prevent washout during the subsequent spin-coating processes. By varying the thickness of the MoO₃ layer from 0 to 4 nm, we engineered the interfacial properties of the graphene electrode such as wettability and doping level.^[18,32]

The wettability of PEDOT:PSS on graphene and ITO surfaces was crucial for fabricating high performance devices, and it was investigated without and with a MoO₃ layer using a contact angle measurement. **Figure 2** shows the optical microscopy images of PEDOT:PSS droplets dripped onto the surfaces of graphene and ITO, and the insets show the optical images of PEDOT:PSS/MAPbI₃ deposited on the glass/graphene substrates. Without a MoO₃ layer, as shown in Figure 2a, the contact angle of the PEDOT:PSS was measured as 90.4° ± 0.3° on graphene surface, on which, consequently, continuous PEDOT:PSS/MAPbI₃ layers were hardly formed by a spin-coating

process (inset, Figure 2a). With a 1 nm thick MoO₃ layer on graphene, however, the contact angle was reduced to 46.6° ± 1.3°, and further to 30.0° ± 1.6° with a 2 nm thick MoO₃ layer, as shown in Figure 2b,c, respectively. The improved wettability by the MoO₃ layers also can be confirmed from the insets of Figure 2b,c. The dark brownish MAPbI₃ films were observed to be well formed in a square shape at the center of the glass substrates where the MoO₃ layers were deposited by thermal evaporation in advance. Particularly, a very clear square-shaped MAPbI₃ film was formed on the 2 nm thick MoO₃ layer, indicating better wetting of PEDOT:PSS on the thicker MoO₃ layer (see inset of Figure 2c). The scanning electron microscopy (SEM) images in Figure S1 (Supporting Information) clearly show that the hydrophobic graphene surface, which was not covered sufficiently by the 1 nm thick MoO₃ layer, became almost completely covered by the 2 nm thick MoO₃ layer. For comparison, the contact angles of PEDOT:PSS on ITO surfaces were also measured before and after the combined treatment of ultraviolet/ozone (UVO) and MoO₃ deposition, as shown in Figure 2d–f. Similar to graphene, the as-prepared ITO surface was not wettable for PEDOT:PSS to form a continuous film by spin coating. Applying UVO treatment to the ITO surface, the contact angle was considerably decreased from 84.0° ± 1.3° (Figure 2d) to 16.9° ± 1.8° (Figure 2e), and slightly further to 9.3° ± 0.6° (Figure 2f) with the 1 nm thick MoO₃ layer, which implies improved hydrophilicity of the ITO surfaces.

Figure 3 shows the cross-sectional SEM images of the fabricated devices employing the graphene electrode with 2 nm thick MoO₃ (Figure 3a) and the ITO electrode with 1 nm thick MoO₃ (Figure 3b). The images on the left-hand side were measured in the secondary electron (SE) mode, and on the right-hand side were measured in back-scattered electron (BSE) mode. The hydrophilicity imposed by the MoO₃ interfacial layer allows for a smooth and continuous formation of the PEDOT:PSS by spin coating on both graphene and ITO with similar thickness (≈50 nm) and morphology. In addition, the surfaces of the perovskite films were observed to be quite smooth with similar thickness (≈510 nm) in both cases as shown in Figure 3. These smooth and dense perovskite films were fabricated via Lewis base adduct of PbI₂ that we recently developed to create highly reproducible n–i–p perovskite solar cells with the best PCE of 19.7%.^[33] CH₃NH₃I (MAI)•PbI₂•dimethyl sulfoxide (DMSO) adduct films were first formed by spin-coating with dripping diethyl ether to wash out the surplus dimethylformamide (DMF) solvent, and then were transformed to the perovskite films through annealing.

In order to investigate the influence of the MoO₃ thickness on the device performance, MoO₃ layers with four different thicknesses (0, 1, 2, and 4 nm) were employed to both graphene and ITO electrodes. The resultant photovoltaic properties of the devices are summarized in **Table 1**, and the relationship between the average PCE and the thickness of the

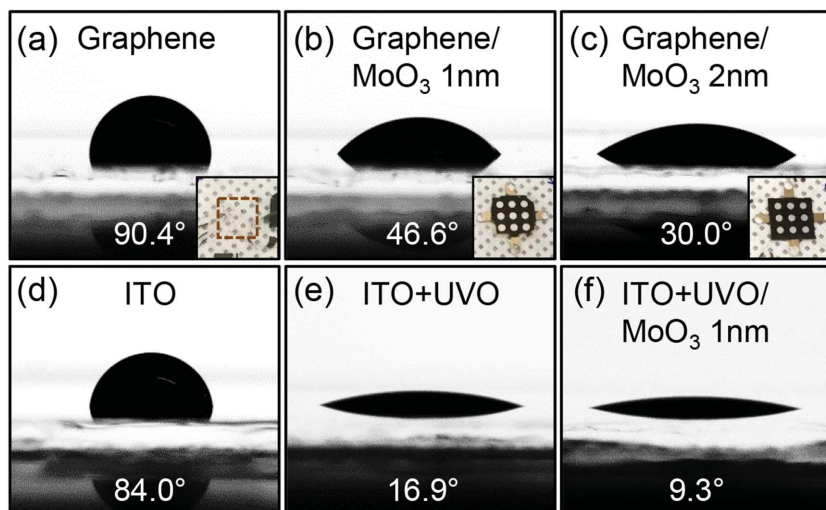


Figure 2. Droplets of PEDOT:PSS on a) as-prepared graphene, b) graphene covered with 1 nm MoO₃, c) graphene covered with 2 nm MoO₃, d) as-prepared ITO, e) UVO-treated ITO, and f) ITO covered with 1 nm MoO₃ after UVO treatment. Enhanced wetting of PEDOT:PSS on both graphene and ITO surfaces was observed after thermal deposition of the MoO₃ layers. The insets in (ac) show the optical images of PEDOT:PSS/MAPbI₃ films fabricated on the corresponding glass/graphene surfaces. The MoO₃ layers were preformed in a square shape at the center of the substrates before spin coating those PEDOT:PSS/MAPbI₃ films.

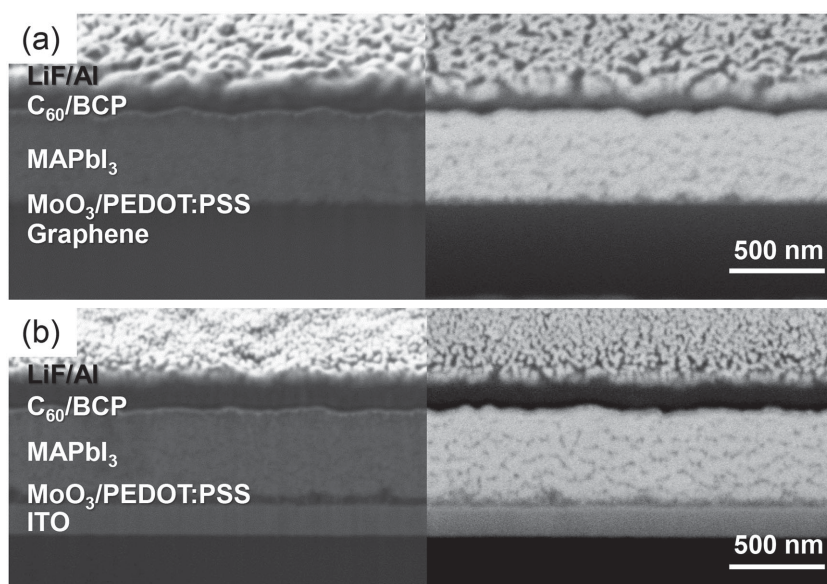


Figure 3. Cross-sectional SEM images of the devices employing a) graphene/2 nm MoO₃ electrode and b) ITO/1 nm MoO₃ electrode measured in SE mode (left) and BSE mode (right).

MoO₃ layer is depicted in **Figure 4a,b** for graphene and ITO electrodes, respectively. For convenience, the electrodes modified by the MoO₃ layers were named as G-M0, G-M1, G-M2, G-M4, ITO-M0, ITO-M1, ITO-M2, and ITO-M4, where the number refers to the thickness of the MoO₃ layer in nanometer, G and ITO refer to the graphene and the ITO electrodes, respectively.

In the case of the graphene-based devices, as shown in **Figure 4a**, the PCEs of the G-M0 devices could not be evaluated because neither the PEDOT:PSS nor perovskite solutions wetted the hydrophobic graphene surfaces to form films after spin-coating (also see inset of **Figure 2a**). Even the G-M1 devices exhibited large variation in the PCEs from 0% to 12.1%, which was attributed to a nonuniform coating of PEDOT:PSS on the G-M1 surface. As addressed earlier, the 1 nm thick MoO₃ layer failed to cover the hydrophobic graphene surface thoroughly. As a result, the current density and voltage (*J*-*V*) characteristics were not consistent among devices (see **Figure S2a**, Supporting Information). With thicker MoO₃ layers than 1 nm, however, variations in performances among devices became significantly alleviated (see **Figure 4a** and **Figure S2b**, Supporting Information), resulting in the average PCEs of 16.1% and 15.9% with

the G-M2 and the G-M4 devices, respectively. From the G-M2 device, the highest PCE of 17.1% was achieved, and, to the best of our knowledge, this is not only the first demonstration of graphene electrodes in perovskite-based solar cells substituting for common TCO electrodes, but also the highest efficiency reported for TCO-free solar cells. For comparison, devices with the same structure but with the ITO electrode were investigated with varied MoO₃ thickness. As shown in **Figure 4b** for the ITO-based devices, the PCE was affected noticeably by a few nanometer changes of the MoO₃ thickness. Utilizing ITO-M1 instead of ITO-M0 electrode increases the average PCE from 17.0% to 18.2%. With the MoO₃ layers thicker than 1 nm, the average PCE of the ITO-M2 and ITO-M4 devices were reduced to 16.1% and 14.7%, respectively. The histogram of the PCEs for each electrode type, G-M2 and ITO-M1, was obtained as shown in **Figure S3** (Supporting Information).

The *J*-*V* curves for the best-performing G-M2 and ITO-M1 devices under air mass 1.5 global (AM 1.5G) one sun illumination at 100 mW cm⁻² were exhibited in **Figure 4c,d**, respectively, measured via reverse and forward bias sweep. Both the G-M2 and ITO-M1 devices did not show significant hysteresis by the voltage scan directions, which was similar to the behaviors of the reported solar cells with inverted architecture in other literatures.^[14,15] In addition, higher series resistance and lower shunt resistance of the G-M2 device compared to the ITO-M1 device are clearly shown in these figures. To understand the electrical properties of the MoO₃-modified graphene and ITO electrodes, the sheet resistance was measured by a four-point probe. **Figure 4e** shows the relationship between the sheet resistance and the thickness of the MoO₃ layer for graphene and ITO. As shown, the initially high sheet resistance of the as-prepared graphene (>2 kΩ cm²) on a glass substrate was remarkably reduced to ≈780 Ω cm² by depositing only a 0.5 nm thick MoO₃ layer, and decreased further up to ≈500 Ω cm² by increasing the thickness of the MoO₃ layer to 2 nm. The sheet resistance of the as-prepared bare ITO was measured as 9.5 Ω cm² and slightly decreased to 9.2 Ω cm² as depositing 1 and 2 nm thick MoO₃ layers. Although the sheet resistance of the initial

Table 1. Photovoltaic parameters of the graphene- and ITO-based devices with MoO₃ layers of varying thickness.

Sample ID	Electrode	MoO ₃ thickness [nm]	V _{oc} [V]	J _{sc} [mA cm ⁻²]	FF	PCE [%]	Best PCE [%]
G-M1	Graphene	1	0.72 ± 0.36	17.6 ± 6.3	0.45 ± 0.09	6.7 ± 4.2	12.1
G-M2		2	1.03 ± 0.02	21.9 ± 0.4	0.72 ± 0.02	16.1 ± 0.6	17.1
G-M4		4	1.00 ± 0.01	22.9 ± 0.4	0.70 ± 0.02	15.9 ± 0.5	16.2
ITO-M0		ITO	0	0.96 ± 0.01	21.4 ± 0.5	0.83 ± 0.02	17.0 ± 0.4
ITO-M1	1		0.97 ± 0.01	22.6 ± 0.4	0.83 ± 0.01	18.2 ± 0.5	18.8
ITO-M2	2		0.95 ± 0.01	22.2 ± 0.4	0.76 ± 0.01	16.1 ± 0.4	16.9
ITO-M4	4		0.94 ± 0.01	21.0 ± 0.4	0.74 ± 0.01	14.7 ± 0.6	15.7

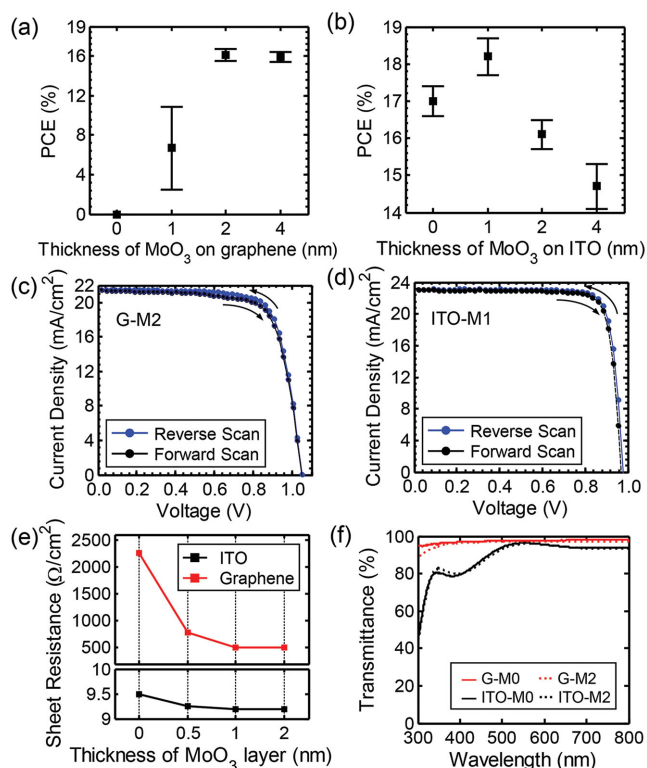


Figure 4. a,b) Relationship between average PCE and MoO₃ thickness for a) graphene electrodes and b) ITO electrodes. c,d) *J*-*V* curves for best-performing c) G-M2 and d) ITO-M1 devices under AM 1.5G illumination at 100 mW cm⁻² measured via reverse (blue) and forward (black) bias sweep. e) Relationship between sheet resistance and MoO₃ thickness for graphene and ITO. f) Transmittance of graphene and ITO with/without 2 nm thick MoO₃ layers.

single-layer graphene was considerably decreased by over four-fold owing to the MoO₃ doping, it was still much higher than that of ITO, which resulted in higher series resistance, lower shunt resistance, and lower fill factor (FF) of the G-M2 device than those of the ITO-M1 device. Nevertheless, the G-M2 device exhibited a comparable short-circuit current (*J*_{sc}) value to the ITO-M1 device due to higher transparency (≈97% transmittance) of the one-atom-thick single-layer graphene than ITO (≈89%) over the visible wavelength range, as shown in Figure 4f. The external quantum efficiency (EQE) spectra for the best-performing G-M2 and ITO-M2 devices were shown in Figure S4 (Supporting Information), from which the integrated photocurrents were calculated as 20.2 and 21.0 mA cm⁻², respectively. The EQEs of graphene- and ITO-based devices were similar because the lower carrier collection efficiency of the graphene anode was compensated by its higher optical transmittance (see Figure 4f and Figure S5, Supporting Information) compared to the ITO anode.

Furthermore, the G-M2 device showed higher open-circuit voltage (*V*_{oc}) value than that of the ITO-M1 device, which contributed to the high PCE of the G-M2 device (higher than 90% of that of the ITO-M1 device) despite graphene's much lower conductivity than ITO. Given the same device structure but electrode, their *V*_{oc} difference may be related to the work function differences in the electrodes. To investigate the effect of the ultrathin MoO₃ layer on the work function of the ITO

and graphene electrodes, ultraviolet photoelectron spectroscopy (UPS) measurements were carried out. Figure 5 shows the UPS spectra of the ITO and the graphene electrodes with the MoO₃ layers of varying thickness. As shown in Figure 5a, the deposition of a 0.5 nm thick MoO₃ layer rapidly shifted the secondary electron cutoff of the as-prepared ITO to a higher kinetic energy, indicating the increase of the work function from 4.29 to 4.65 eV. Further deposition of the MoO₃ layer to 1 and 2 nm in thickness elevated the work function slightly to 4.69 and 4.72 eV, respectively. It is desirable to minimize the energy barrier between the anode and the HTL for efficient hole-collection. As shown in the Table 1, the higher *J*_{sc} and the PCE of the ITO-M1 device than those of the ITO-M0 device were mainly attributed to the increased work function of the electrode, inducing improved hole-collection efficiency. On the other hand, the PCEs decreased as the thickness of the MoO₃ layer increased to 2 and 4 nm. Although thermally evaporated MoO₃ possesses very deep valence band edge, holes can be transported through gap states in the MoO₃ band structure formed near metal contact.^[34,35] The hole-collection efficiency of the ITO-M2 and ITO-M4 devices was likely enhanced due to a slight increase in the work function of the electrode by MoO₃, however, ITO/MoO₃/PEDOT:PSS with a thicker MoO₃ layer lacking gap states would not facilitate quasi-ohmic contact for efficient hole extraction,^[35,36] which resulted in decreased PCE of the ITO-M2 and ITO-M4 devices.

The UPS spectra of the graphene-based devices also showed a similar behavior to that of the ITO devices with the deposition of the MoO₃ layer. As shown in Figure 5b, a rapid shift of the onset of photoemission was observed on depositing a 0.5 nm

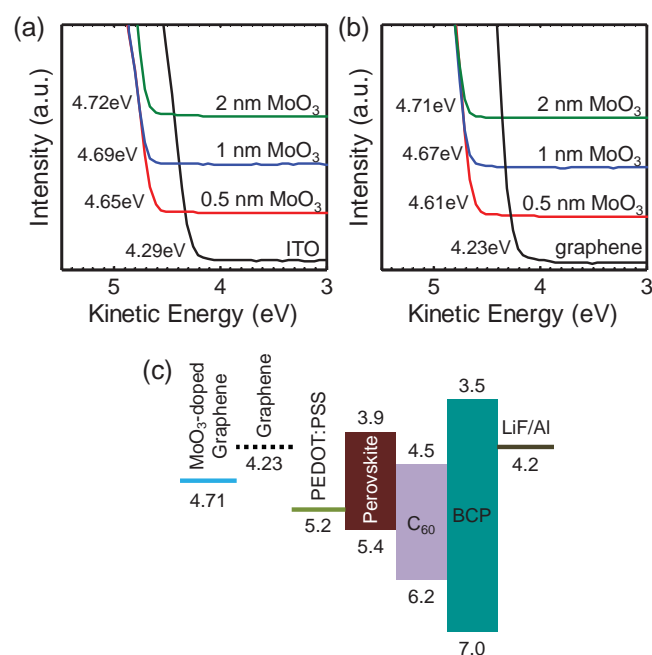


Figure 5. a,b) UPS spectra and calculated work functions of (a) ITO and (b) graphene with MoO₃ layers of varying thickness. c) Schematic energy level diagram of the fabricated inverted structure. The energy levels are taken from Jeng et al.^[44] The work function of as-prepared graphene (denoted by black dashed line, 4.23 eV) was increased to 4.71 eV by MoO₃ doping (denoted by blue solid line).

thick MoO₃ layer on the as-prepared graphene, indicating the increase of the work function from 4.23 to 4.61 eV. Further deposition of the MoO₃ layer to 1 and 2 nm in thickness increased the work function slightly to 4.67 and 4.71 eV, respectively. As illustrated in Figure 5c, the ultrathin MoO₃ layer deposited on graphene consequently facilitated hole collection from the HTL to the graphene anode by reducing the energy barrier at the interface, as well as allowing the PEDOT:PSS film to be successfully spin-coated on the hydrophobic graphene surfaces. Comparing the UPS data for the ITO and the graphene electrodes, the work functions with the same MoO₃ thickness were found to be almost the same. The work function values of the ITO-M1 and G-M2 electrodes also showed no significant difference, implying that the higher V_{oc} of the G-M2 device than that of the ITO-M1 device could not be explained in terms of the energy barrier difference at the anode/HTL interfaces.

Since V_{oc} also can be influenced by the interface quality, atomic force microscopy (AFM) measurement was carried out to study the morphology of the electrodes after the formation of the MoO₃ and the PEDOT:PSS films. As shown in Figure S6a–c (Supporting Information), the surface root-mean-square (rms) roughnesses for G-M0, G-M2, and G-M2/PEDOT:PSS were measured as 0.47, 0.29, and 0.98 nm, respectively. The rms roughnesses for ITO-M0, ITO-M1, and ITO-M1/PEDOT:PSS were found to be 2.06, 1.95, and 1.21 nm, respectively, as shown in Figure S6d–f (Supporting Information). It is noticeable here that G-M2 showed more than sixfold lower surface rms roughness of 0.29 nm than that of ITO-M1 (1.95 nm rms roughness). From the literature,^[37] it is known that better interface can be created between stacked layers when the surface roughness of the underlying layer is smaller, which consequently increases V_{oc} . In this respect, the G-M2 electrode seemed to have established better interfaces with PEDOT:PSS than ITO-M1/PEDOT:PSS interfaces, contributing to the higher V_{oc} of the G-M2 devices.

Moreover, it was observed from the SEM images of the perovskite surfaces formed on G-M2/PEDOT:PSS and ITO-M1/PEDOT:PSS, as shown in Figure S7 (Supporting Information), that the overall grain size of the former was larger than that of the latter. The X-ray diffraction patterns of the perovskite films fabricated on G-M2/PEDOT:PSS and ITO-M1/PEDOT:PSS also provided information on the difference in grain size. It is noticeable in Figure S8 (Supporting Information) that the peak intensities of the (110) and (220) planes for the G-M2 sample are much stronger than those for the ITO-M1 sample. Recently, it was reported that abnormal grain growth behavior of a perovskite film involved a preferred grain orientation.^[38,39] In our work, the well-oriented grains on graphene electrode were most likely originated from the smaller surface roughness of the underlying layer of the perovskite film. The nanoscale edges of the surface of the underlying layer could serve as nucleation sites and induce formation of randomly oriented grains. In this respect, the grains of the perovskite film on the smoother G-M2/PEDOT:PSS surface could grow to a larger size than those on the ITO-M1/PEDOT:PSS surface. Furthermore, the well-oriented larger grains of the G-M2 devices can be regarded as another factor for the higher V_{oc} in the G-M2 devices compared to the ITO-M1 devices due to reduction in defect-assisted recombination loss at grain boundaries.^[40–42]

We have demonstrated not only the first perovskite solar cells adopting graphene as a transparent conducting anode but also

the highest efficiency TCO-free solar cells. Both graphene- and ITO-based inverted devices with the insertion of thin MoO₃ interfacial layers have been fabricated for comparison. Interfacial engineering by introducing a MoO₃ layer on the anode surface enables a better interface formation and a desirable energy level alignment between the anode and the HTL. In particular, MoO₃ dopes holes into graphene to better serve as a conducting electrode. With the optimized thickness of the MoO₃ layer, best PCEs of 17.1% and 18.8% have been achieved with the graphene- and the ITO-based devices, respectively. The significantly lower conductivity of the graphene electrode than that of the ITO electrode is compensated by graphene's higher transparency and lower surface roughness, resulting in comparable J_{sc} , higher V_{oc} , and consequently >90% PCE of the graphene device compared to the ITO device. We believe that the present work highlights the great potential of graphene as a transparent electrode and provides new insights into future studies for developing robust flexible solar cells with high efficiency.

Experimental Section

Solar Cell Fabrication: The graphene devices were fabricated on a commercially available single-layer graphene-coated glass substrates (Graphene Square Inc., >1 k Ω cm², 15 × 15 mm²), which were provided by transferring the CVD-grown graphene on a copper foil to the cleaned glass substrates (AMG, 25 × 25 mm²).^[43] The ITO devices were fabricated on a commercially obtained ITO-coated glass substrates (AMG, 9.5 Ω cm², 25 × 25 mm²). The graphene-coated glass substrates were used as received, and the ITO-coated glass substrates were used after sequential cleaning in acetone, isopropanol, and deionized water using an ultrasonic bath (15 min each), followed by drying with nitrogen gas and storing in an oven at 120 °C. Right before use, the ITO-coated glass substrates were subjected to UVO treatment for 30 min.

The ultrathin MoO₃ layers with varying thickness from 1 to 4 nm were fabricated on the graphene- or ITO-coated glass substrates at deposition rate of 0.1 Å s⁻¹ using a vacuum thermal evaporator, followed by an annealing at 150 °C for 10 min. The deposition rate and the thickness were monitored by a quartz crystal sensor during the deposition. To prepare a highly uniform PEDOT:PSS (Clevios P VP Al 4083) HTL, the substrates were pretreated with deionized water, and the PEDOT:PSS solution of 50 μ L was dropped onto the rotating substrates right after starting the spin-coating process at 5000 rpm for 30 s. The MAPbI₃ perovskite layers were fabricated via Lewis base adduct method described by Ahn et al.^[33] A 1:1:1 molar ratio mixture of PbI₂ (Alfa Aesar), MAI (MAI was synthesized by the method in refs. [2] and [3] and DMSO (Sigma-Aldrich) was dissolved in DMF at 50 wt% without heating. The fully dissolved solution was spin coated onto the PEDOT:PSS layer at 3500 rpm for 20 s, with a dropping of 0.3 mL diethyl ether 8 s after starting the spin-coating process. The transparent green film, so called CH₃NH₃I•PbI₂•DMSO adduct film, changed to a dark brownish perovskite film by heating at 65 °C for 1 min and 100 °C for 4 min. After that, the C₆₀ (20 nm), BCP (10 nm), LiF (0.5 nm), and Al (150 nm) were thermally deposited on the substrates inside the vacuum thermal evaporator under <10⁻⁶ Torr. All the spin-coating processes were carried out in ambient condition.

Characterization: SEM images were obtained using field-emission scanning electron microscopy (AURIGA, Zeiss) and the cross-sectional images were obtained using the same equipment from the samples milled by focused ion beam. Solar simulated AM 1.5G sunlight was generated with Oriol Sol3A solar simulator calibrated to give 100 mW cm⁻² using a standard Si photovoltaic cell (RC-1000-TC-KG5-N, VLSI Standards). J - V curves were recorded with a Keithley 2400 source meter. The forward and reverse scan rate was set to 200 ms per 20 mV. The active area of the devices is 1.77 mm². EQE spectra were measured with a Newport IQE200 system equipped with a 300 mW Xenon light

source and a lock-in amplifier. Sheet resistance was measured using a four-point probe (CMT-SERIES, Advanced Instrument Technology). Transmittance was measured by UV-vis spectroscopy (Cary 5000, Agilent). UPS measurement was carried out by using a He discharge lamp (He I 21.2 eV, AXIS-NOVA, Kratos). AFM images were obtained using a XE-100 (Park Systems) scanning probe microscope in noncontact mode.

Supporting Information

Supporting Information is available from the Wiley Online Library or from the author.

Acknowledgements

H.S. and N.A. contributed equally to this work. This work was supported by the Global Frontier R&D Program on Center for Multiscale Energy System funded by the National Research Foundation under the Ministry of Science, ICT and Future Planning, Korea (2011-0031561, 2012M3A6A7054855, 2014M3A6A7060584, and 2012M3A6A7054861). The authors thank Jin-Wook Lee for his kind help in measurement of photoluminescence spectra and discussions.

Received: September 18, 2015

Revised: October 26, 2015

Published online: December 3, 2015

- [1] A. Kojima, K. Teshima, Y. Shirai, T. Miyasaka, *J. Am. Chem. Soc.* **2009**, *131*, 6050.
- [2] J.-H. Im, C.-R. Lee, J.-W. Lee, S.-W. Park, N.-G. Park, *Nanoscale* **2011**, *3*, 4088.
- [3] H.-S. Kim, C.-R. Lee, J.-H. Im, K.-B. Lee, T. Moehl, A. Marchioro, S.-J. Moon, R. Humphry-Baker, J.-H. Yum, J. E. Moser, M. Grätzel, N.-G. Park, *Sci. Rep.* **2012**, *2*, 591.
- [4] G. Xing, N. Mathews, S. Sun, S. S. Lim, Y. M. Lam, M. Grätzel, S. Mhaisalkar, T. C. Sum, *Science* **2013**, *342*, 344.
- [5] P. Docampo, J. M. Ball, M. Darwich, G. E. Eperon, H. J. Snaith, *Nat. Commun.* **2013**, *4*, 2761.
- [6] S. D. Stranks, G. E. Eperon, G. Grancini, C. Menelaou, M. J. P. Alcocer, T. Leijtens, L. M. Herz, A. Petrozza, H. J. Snaith, *Science* **2013**, *342*, 341.
- [7] W. Ke, G. Fang, J. Wan, H. Tao, Q. Liu, L. Xiong, P. Qin, J. Wang, H. Lei, G. Yang, M. Qin, X. Zhao, Y. Yan, *Nat. Commun.* **2015**, *6*, 6700.
- [8] W. Ke, G. Fang, Q. Liu, L. Xiong, P. Qin, H. Tao, J. Wang, H. Lei, B. Li, J. Wan, G. Yang, Y. Yan, *J. Am. Chem. Soc.* **2015**, *137*, 6730.
- [9] J. M. Ball, M. M. Lee, A. Hey, H. J. Snaith, *Energy Environ. Sci.* **2013**, *6*, 1739.
- [10] J. H. Heo, S. H. Im, J. H. Noh, T. N. Mandal, C.-S. Lim, J. A. Chang, Y. H. Lee, H. Kim, A. Sarkar, K. Nazeeruddin Md, M. Grätzel, S. I. Seok, *Nat. Photonics* **2013**, *7*, 486.
- [11] G. E. Eperon, V. M. Burlakov, P. Docampo, A. Goriely, H. J. Snaith, *Adv. Funct. Mater.* **2014**, *24*, 151.
- [12] O. Malinkiewicz, A. Yella, Y. H. Lee, G. M. Espallargas, M. Grätzel, M. K. Nazeeruddin, H. J. Bolink, *Nat. Photonics* **2014**, *8*, 128.
- [13] J. You, Z. Hong, Y. Yang, Q. Chen, M. Cai, T.-B. Song, C.-C. Chen, S. Lu, Y. Liu, H. Zhou, Y. Yang, *ACS Nano* **2014**, *8*, 1674.
- [14] J. Seo, S. Park, Y. Chan Kim, N. J. Jeon, J. H. Noh, S. C. Yoon, S. I. Seok, *Energy Environ. Sci.* **2014**, *7*, 2642.
- [15] J. H. Heo, H. J. Han, D. Kim, T. K. Ahn, S. H. Im, *Energy Environ. Sci.* **2015**, *8*, 1602.
- [16] B. J. Kim, D. H. Kim, Y.-Y. Lee, H.-W. Shin, G. S. Han, J. S. Hong, K. Mahmood, T. K. Ahn, Y.-C. Joo, K. S. Hong, N.-G. Park, S. Lee, H. S. Jung, *Energy Environ. Sci.* **2015**, *8*, 916.
- [17] J. Wu, H. A. Becerril, Z. Bao, Z. Liu, Y. Chen, P. Peumans, *Appl. Phys. Lett.* **2008**, *92*, 263302.
- [18] Y. Wang, S. W. Tong, X. F. Xu, B. Özyilmaz, K. P. Loh, *Adv. Mater.* **2011**, *23*, 1514.
- [19] H. Park, S. Chang, X. Zhou, J. Kong, T. Palacios, S. Gradecak, *Nano Lett.* **2014**, *14*, 5148.
- [20] A. R. b. M. Yusoff, D. Kim, F. K. Schneider, W. J. da Silva, J. Jang, *Energy Environ. Sci.* **2015**, *8*, 1523.
- [21] M. W. Rowell, M. A. Topinka, M. D. McGehee, H.-J. Prall, G. Dennler, N. S. Sariciftci, L. Hu, G. Gruner, *Appl. Phys. Lett.* **2006**, *88*, 233506.
- [22] I. Jeon, K. Cui, T. Chiba, A. Anisimov, A. G. Nasibulin, E. I. Kauppinen, S. Maruyama, Y. Matsuo, *J. Am. Chem. Soc.* **2015**, *137*, 7982.
- [23] R. V. Salvatierra, C. E. Cava, L. S. Roman, A. J. G. Zabin, *Adv. Funct. Mater.* **2013**, *23*, 1490.
- [24] B. Muhsin, R. Roesch, G. Gobsch, H. Hoppe, *Sol. Energy Mater. Sol. Cells* **2014**, *130*, 551.
- [25] J. Zou, H.-L. Yip, S. K. Hau, A. K.-Y. Jen, *Appl. Phys. Lett.* **2010**, *96*, 203301.
- [26] M. Song, H.-J. Kim, C. S. Kim, J.-H. Jeong, C. Cho, J.-Y. Lee, S.-H. Jin, D.-G. Choi, D.-H. Kim, *J. Mater. Chem. A* **2015**, *3*, 65.
- [27] Y. H. Kim, C. Sachse, M. L. Machala, C. May, L. Müller-Meskamp, K. Leo, *Adv. Funct. Mater.* **2011**, *21*, 1076.
- [28] W. Zhang, B. Zhao, Z. He, X. Zhao, H. Wang, S. Yang, H. Wu, Y. Cao, *Energy Environ. Sci.* **2013**, *6*, 1956.
- [29] K. Sun, P. Li, Y. Xia, J. Chang, J. Ouyang, *ACS Appl. Mater. Inter.* **2015**, *7*, 15314.
- [30] P. You, Z. Liu, Q. Tai, S. Liu, F. Yan, *Adv. Mater.* **2015**, *27*, 3632.
- [31] K. Yan, Z. Wei, J. Li, H. Chen, Y. Yi, X. Zheng, X. Long, Z. Wang, J. Wang, J. Xu, S. Yang, *Small* **2015**, *11*, 2269.
- [32] J. Meyer, P. R. Kidambi, B. C. Bayer, C. Weijtens, A. Kuhn, A. Centeno, A. Pesquera, A. Zurutuza, J. Robertson, S. Hofmann, *Sci. Rep.* **2014**, *4*, 5380.
- [33] N. Ahn, D.-Y. Son, I.-H. Jang, S. M. Kang, M. Choi, N.-G. Park, *J. Am. Chem. Soc.* **2015**, *137*, 8696.
- [34] P. Qin, G. Fang, W. Ke, F. Cheng, Q. Zheng, J. Wan, H. Lei, X. Zhao, *J. Mater. Chem. A* **2014**, *2*, 2742.
- [35] M. T. Greiner, L. Chai, M. G. Helander, W.-M. Tang, Z.-H. Lu, *Adv. Funct. Mater.* **2013**, *23*, 215.
- [36] Z. Liu, M. Kobayashi, B. C. Paul, Z. Bao, Y. Nishi, *Phys. Rev. B* **2010**, *82*, 035311.
- [37] N. Kang, M. Hoang, D. Choi, B.-K. Ju, J.-M. Hong, J.-W. Yu, *Macromol. Res.* **2013**, *21*, 65.
- [38] Q. Dong, Y. Yuan, Y. Shao, Y. Fang, Q. Wang, J. Huang, *Energy Environ. Sci.* **2015**, *8*, 2464.
- [39] W. S. Yang, J. H. Noh, N. J. Jeon, Y. C. Kim, S. Ryu, J. Seo, S. I. Seok, *Science* **2015**, *348*, 1234.
- [40] W. Nie, H. Tsai, R. Asadpour, J.-C. Blancon, A. J. Neukirch, G. Gupta, J. J. Crochet, M. Chhowalla, S. Tretiak, M. A. Alam, H.-L. Wang, A. D. Mohite, *Science* **2015**, *347*, 522.
- [41] J. You, Y. Yang, Z. Hong, T.-B. Song, L. Meng, Y. Liu, C. Jiang, H. Zhou, W.-H. Chang, G. Li, Y. Yang, *Appl. Phys. Lett.* **2014**, *105*, 183902.
- [42] Q. Chen, H. Zhou, Z. Hong, S. Luo, H.-S. Duan, H.-H. Wang, Y. Liu, G. Li, Y. Yang, *J. Am. Chem. Soc.* **2014**, *136*, 622.
- [43] W. H. Lee, J. Park, S. H. Sim, S. B. Jo, K. S. Kim, B. H. Hong, K. Cho, *Adv. Mater.* **2011**, *23*, 1752.
- [44] J.-Y. Jeng, Y.-F. Chiang, M.-H. Lee, S.-R. Peng, T.-F. Guo, P. Chen, T.-C. Wen, *Adv. Mater.* **2013**, *25*, 3727.